

LISA Sensitivity to Gravitational Waves from Sound Waves

Kai Schmitz

Theoretical Physics Department, CERN, 1211 Geneva 23, Switzerland

E-mail: kai.schmitz@cern.ch

Abstract. *Gravitational waves* (GWs) produced by sound waves in the primordial plasma during a strong first-order phase transition in the early Universe are going to be a main target of the upcoming *Laser Interferometer Space Antenna* (LISA) experiment. In this short note, I draw a global picture of LISA's expected sensitivity to this type of GW signal, based on the concept of *peak-integrated sensitivity curves* (PISCs) recently introduced in Refs. [1, 2]. In particular, I use LISA's PISC to perform a systematic comparison of several thousands of benchmark points in ten different particle physics models in a compact fashion. The presented analysis (i) retains the complete information on the optimal signal-to-noise ratio, (ii) allows for different power-law indices describing the spectral shape of the signal, (iii) accounts for galactic confusion noise from compact binaries, and (iv) exhibits the dependence of the expected sensitivity on the collected amount of data. An important outcome of this analysis is that, for the considered set of models, galactic confusion noise typically reduces the number of observable scenarios by roughly a factor two, more or less independent of the observing time. The numerical results presented in this paper are also available on Zenodo [3].

Contents

1	Introduction	1
2	Signal	2
3	Noise	5
4	Sensitivity	7
5	Conclusions	11

1 Introduction

Being the first experiment that is going to measure *gravitational waves* (GWs) in the milli-Hertz range, the *Laser Interferometer Space Antenna* (LISA) [4, 5] is set to open a new observational window onto the Universe. Among the possible GW signals in the LISA frequency band, the stochastic GW background [6–9] from a *strong first-order phase transition* (SFOPT) in the early Universe [10, 11] represents a particularly well-motivated example that is expected in many extensions of the standard model of particle physics (see, *e.g.*, the two review reports by the LISA Cosmology Working Group [12, 13]). In this paper, we will discuss LISA’s projected sensitivity to this type of signal from a bird’s eye view, focusing on the contribution from plasma sound waves that are generated during the phase transition [14–20]. Other possible contributions to the GW signal from a cosmological phase transition include the collision of vacuum bubbles [21–26] and magnetohydrodynamic turbulence [27–32]. The former, however, is negligibly small in most cases, while the latter presently still demands a better theoretical understanding. Restricting ourselves to the sound-wave contribution to the GW signal therefore represents a conservative approach (see also the discussion in Ref. [13]).

The main goal of this paper is to draw a global picture of LISA’s sensitivity to the acoustic GW signal from a SFOPT across a large range of different particle physics models. Remarkably enough, the standard approaches to this problem suffer from various limitations that make it difficult to scale up the number of benchmark points and / or models that are to be included in the analysis. A simple comparison of theoretically computed GW spectra with LISA’s power-law-integrated sensitivity curve [33], *e.g.*, does not preserve any information on the expected *signal-to-noise ratio* (SNR), simply because the signal is not a pure power law, and quickly becomes impractical for a large number of spectra. An analysis of the expected SNR as a function of the underlying SFOPT parameters α , β/H , T_* , etc. (see Sec. 2), on the other hand, is complicated by the high dimensionality d of parameter space. In practice, one therefore often resorts to hypersurfaces in parameter space, keeping $d - 2$ parameters fixed at characteristic values that roughly approximate the true values for the individual benchmark points that one is interested in. This procedure may be useful as long as one considers one model at a time; however, it becomes impractical as soon as one intends to compare different models to each other that live on vastly separated hypersurfaces in parameter space. In this paper, in order to avoid these limitations, we will therefore make use of the concept of *peak-integrated sensitivity curves* (PISCs) that was recently introduced in Refs. [1, 2]. The key idea behind the PISC approach is to project the expected sensitivity of a given

experiment not into the space of SFOPT parameters but into the space of observables that will eventually be part of the experimental data analysis. The acoustic GW signal from a SFOPT is primarily described by two such observables: (i) a peak frequency f_{peak} , where the GW amplitude reaches a local maximum, and (ii) the GW amplitude at this frequency itself, Ω_{peak} , or equivalently, the integrated GW energy density, Ω_{tot} (see Sec. 2). The PISC that we will discuss in this paper, LISA’s PISC for acoustic GWs, is thus defined as the experimental sensitivity curve in the two-dimensional parameter space spanned by f_{peak} and Ω_{tot} . As we will show, this curve retains the complete information on the expected SNR and can be constructed in a universal fashion without any reference to a particular model or a specific hypersurface in parameter space. Thanks to these characteristic properties, it serves as an ideal starting point for a systematic comparison of a large number of SFOPT scenarios.

For concreteness, we will consider in this paper the ten particle physics models that were discussed in Ref. [13] (see Sec. 4). In particular, we will reproduce the complete information on the expected SNR for all 3720 individual benchmark points that were studied in Ref. [13] in a single PISC plot. We will then demonstrate how this PISC plot can be used to address several questions for all ten models at the same time. Specifically, we will discuss (i) the importance of *galactic confusion noise* (GCN) from compact binaries [34–38], (ii) the time dependence of LISA’s sensitivity as the mission progresses, and (iii) the impact of varying the spectral shape of the signal. We argue that it is easier and more intuitive to address these questions based on our PISC plot rather than ten model-dependent SNR contour plots on ten different hypersurfaces in parameter space. An important result of our analysis is that roughly half of all SFOPT scenarios that one would claim to be within LISA’s reach in the absence of any GCN actually fail to pass the necessary SNR threshold when GCN is taken into account. We thus conclude that, although this is presently not yet standard practice, GCN should always be accounted for in phenomenological studies of GWs from a SFOPT.

The rest of this paper is organized as follows. In Sec. 2, we will review the computation of the acoustic GW signal from a SFOPT, commenting in particular on the issue of shock formation in the plasma; in Sec. 3, we will compute LISA’s strain noise power spectrum, making use of a novel analytical expression for LISA’s signal response function; and in Sec. 4, we will finally combine all ingredients, construct LISA’s PISC, present our PISC master plot, and address the three questions listed above. Sec. 5 contains our conclusions.

2 Signal

The spectrum of acoustic GWs produced during a SFOPT can be written as

$$\Omega_{\text{signal}}(f) = \Omega_{\text{tot}}(\alpha, \beta/H_*, T_*, v_w) \mathcal{S}(f/f_{\text{peak}}). \quad (2.1)$$

In the following, we will now briefly introduce the different quantities in this expression; a more detailed discussion can be found in Refs. [2, 12, 13]. The frequency-independent factor on the right-hand side of Eq. (2.1), Ω_{tot} , denotes the total energy density of acoustic GWs produced during the phase transition, in units of the critical energy density, $\rho_{\text{crit}} = 3 M_{\text{Pl}}^2 H^2$,

$$\Omega_{\text{tot}} = \min\{1, H_* \tau_{\text{sh}}\} \times 3 \left(\frac{g_\rho^*}{g_\rho^0}\right) \left(\frac{g_s^0}{g_s^*}\right)^{4/3} \Omega_\gamma^0 \tilde{\Omega}(8\pi)^{1/3} \frac{\max\{c_s, v_w\}}{\beta/H_*} K^2. \quad (2.2)$$

Here, g_ρ and g_s count the effective numbers of relativistic degrees of freedom that contribute to the radiation energy density ρ_{rad} and entropy density s_{rad} , respectively. The superscript

on these quantities indicates whether they are evaluated at the present temperature T_0 or at the percolation temperature T_* , which represents the relevant temperature scale for GW production during the phase transition. $\Omega_\gamma^0 \simeq 2.47 \times 10^{-5}/h^2$ quantifies the current photon energy density, where h is the dimensionless Hubble parameter in the present epoch, which is defined via the relation $H_0 = 100 h \text{ km/s/Mpc}$. $\tilde{\Omega}$ quantifies the efficiency of GW production from sound waves and follows from integrating the shear stress unequal-time correlator of the bulk fluid [17]. The numerical simulations in Ref. [19] show that $\tilde{\Omega}$ is approximately constant for weak phase transitions. Below, we will use $\tilde{\Omega} = 0.012$ as a representative value, which corresponds to one of the benchmark scenarios studied in Ref. [19]. The combination $(8\pi)^{1/3} \max\{c_s, v_w\}/\beta \equiv R_*$ on the right-hand side of Eq. (2.2) represents the mean bubble size, or equivalently, mean bubble separation at the time of percolation.¹ Here, c_s denotes the speed of sound, v_w is the bubble wall velocity in the plasma rest frame, and β is a measure for the (inverse of the) duration of the phase transition. The factor K describes the energy fraction that is converted to kinetic energy of the bulk fluid during the phase transition,

$$K = \frac{\kappa \alpha}{1 + \alpha}, \quad (2.3)$$

where α characterizes the strength of the phase transition and κ is an efficiency factor that can be computed as a function of α and v_w . In our analysis, we will follow Refs. [12, 13] and use the semianalytical fit functions for κ that are provided in Appendix A of Ref. [39].

In passing, we mention that the derivation of Eq. (2.3) in Ref. [39] is based on the so-called bag equation of state, which assumes a relativistic plasma with speed of sound $c_s^2 = 1/3$ in both the broken and the symmetric phase. This assumption, however, may break down in realistic scenarios; see Ref. [40] for a recent analysis that re-evaluates the efficiency factor κ for detonations with $c_s^2 \neq 1/3$ in the broken phase. At present, the exact speed-of-sound profile across the bubble wall is unfortunately not known for most models. In the following, we will therefore stick to the results of Ref. [39] and set $c_s^2 = 1/3$ throughout our analysis.

The overall prefactor $\min\{1, H_*\tau_{\text{sh}}\}$ in Eq. (2.2) accounts for the finite lifetime of the GW source. As stressed in Refs. [41–43], the generation of GWs from sound waves shuts off after a period τ_{sh} , when shocks begin to form, causing the motion of the bulk plasma to turn turbulent. This leads to a suppression of the GW signal from sound waves whenever the time scale τ_{sh} is shorter than a Hubble time. τ_{sh} can be estimated in terms of the mean bubble separation R_* and the enthalpy-weighted root-mean-square of the fluid velocity, \bar{U}_f ,

$$\tau_{\text{sh}} = \frac{R_*}{\bar{U}_f} = (8\pi)^{1/3} \frac{\max\{c_s, v_w\}}{\beta \bar{U}_f}. \quad (2.4)$$

\bar{U}_f is given in terms of the kinetic-energy fraction K and the mean adiabatic index Γ , which is defined as the ratio of the mean enthalpy density \bar{w} and the mean energy density \bar{e} ,

$$\bar{U}_f = \left(\frac{K}{\Gamma}\right)^{1/2} = \left(\frac{3}{4} \frac{\kappa \alpha}{1 + \alpha}\right)^{1/2}, \quad (2.5)$$

where we used that $\Gamma = \bar{w}/\bar{e} = 4/3$ for a relativistic fluid. Alternatively, one may estimate τ_{sh} directly in terms of R_* and K and neglect the mean adiabatic index and the detour via the mean fluid velocity, $\tau_{\text{sh}} = R_*/K^{1/2}$. This is the approach adopted in Ref. [13]. Another

¹Describing the colliding bubbles by a regular cubic lattice of nonoverlapping spheres, the bubble number density at $T = T_*$ is given by $n_B = 1/R_*^3$. Other lattice packings result in slight modifications of this relation.

difference between Ref. [13] and our analysis is that we include a factor 3 in our expression for Ω_{tot} , which is consistent with Ref. [19] (see, in particular, the erratum to this paper), whereas Ref. [13] includes a factor $1/c_s$, which renders the GW signal smaller by a factor $\sqrt{3}$.

The function \mathcal{S} in Eq. (2.1) describes the spectral shape of the GW signal. One typically expects the spectrum to be peaked at a characteristic frequency f_{peak} , which is why it is most convenient to write \mathcal{S} as a function of f/f_{peak} . The peak frequency f_{peak} itself is set by the mean bubble separation R_* . Its appropriately redshifted value in the present Universe reads

$$f_{\text{peak}} \simeq 8.9 \times 10^{-3} \text{ mHz} \left(\frac{z_{\text{peak}}}{10} \right) \left(\frac{\beta/H_*}{\max\{c_s, v_w\}} \right) \left(\frac{100}{g_s^*} \right)^{1/3} \left(\frac{g_\rho^*}{100} \right)^{1/2} \left(\frac{T_*}{100 \text{ GeV}} \right). \quad (2.6)$$

Here, z_{peak} characterizes the hierarchy between R_* and the peak frequency at the time of the phase transition. Its value needs to be inferred from numerical simulations, which indicate that it is generally close to $z_{\text{peak}} = 10$ [19]. The spectral shape function \mathcal{S} is often approximated by a broken power law that scales like f^3 at low frequencies and f^{-4} at high frequencies. This is, in particular, the ansatz chosen by the LISA Cosmology Working Group in Refs. [12, 13]. However, a broken power law of this form is not always necessarily the best choice. The analytical sound shell model of GW production from sound waves in Refs. [18, 20], *e.g.*, predicts an f^5 power law at low frequencies and an f^{-3} power law at high frequencies. Similarly, the outcome of numerical simulations is sometimes better described by an f^{-3} fit rather than an f^{-4} fit at high frequencies [19]. Therefore, in order to account for this variability and uncertainty in the spectral shape function \mathcal{S} , we will go beyond the simple $f^3 \rightarrow f^{-4}$ ansatz and consider a more general class of broken power laws in this paper,

$$\mathcal{S}(x) = \frac{1}{\mathcal{N}} \tilde{\mathcal{S}}(x), \quad \tilde{\mathcal{S}}(x) = \frac{x^p}{[q/(p+q) + p/(p+q)x^n]^{(p+q)/n}}. \quad (2.7)$$

This function is constructed such that it exhibits the following characteristic properties,

$$\mathcal{S}'(x=1) = 0, \quad \mathcal{S}(x=1) = \frac{1}{\mathcal{N}}, \quad \mathcal{S}(x \ll 1) \propto f^p, \quad \mathcal{S}(x \gg 1) \propto f^{-q}. \quad (2.8)$$

We choose the normalization constant \mathcal{N} such that the integral over \mathcal{S} is normalized to unity,

$$\mathcal{N} = \int_{-\infty}^{+\infty} d(\ln x) \tilde{\mathcal{S}}(x) = \left(\frac{q}{p} \right)^{p/n} \left(\frac{p+q}{q} \right)^{(p+q)/n} \frac{\Gamma(p/n) \Gamma(q/n)}{n \Gamma((p+q)/n)}. \quad (2.9)$$

These definitions also allow us to rewrite Eq. (2.1) in terms of the peak amplitude Ω_{peak} ,

$$\Omega_{\text{signal}}(f) = \Omega_{\text{peak}}(\alpha, \beta/H_*, T_*, v_w, p, q, n) \tilde{\mathcal{S}}(f/f_{\text{peak}}), \quad \Omega_{\text{peak}} = \frac{1}{\mathcal{N}} \Omega_{\text{tot}}. \quad (2.10)$$

which illustrates that, unlike the total GW energy density parameter Ω_{tot} , the peak amplitude Ω_{peak} also depends on the values of p , q , and n . In our analysis, we will therefore keep working with Eq. (2.1) and Ω_{tot} , such that the entire dependence on p , q , and n is contained in \mathcal{S} .

In our notation, the standard ansatz for the spectral shape function in Refs. [12, 13] corresponds to $(p, q, n) = (3, 4, 2)$. In this case, the normalization constant \mathcal{N} is given by

$$\mathcal{N}(p=3, q=4, n=2) = \frac{343 \sqrt{7}}{360 \sqrt{3}} \simeq 1.455 \simeq \frac{1}{0.687}. \quad (2.11)$$

In this paper, we will by contrast consider a larger set of (p, q, n) tuples. More specifically, we will work with $p \in \{3, 4, 5\}$, $q \in \{3, 4\}$ and $n \in \{1, 2, 3\}$. Here, our choice of p and q values reflects the range of power laws discussed further above, while the three discrete n values allow us to describe a broad, a mid-sized, and a narrow peak in the spectrum, respectively. In this way, we are able to cover a large range of possible spectral shapes and hence implicitly account for the dependence of p , q , and n on the underlying properties of the phase transition.

3 Noise

Next, we turn to LISA's noise spectrum Ω_{noise} . Again we will restrict ourselves to a brief summary of the basic ingredients; a more comprehensive review can be found in Appendix A of Ref. [2]. Ω_{noise} is defined in terms of LISA's single-sided strain noise spectrum S_{noise} ,

$$\Omega_{\text{noise}}(f) = \frac{2\pi^2}{3H_0^2} f^3 S_{\text{noise}}(f) . \quad (3.1)$$

In our analysis in this paper, we will consider two independent contributions to S_{noise} : LISA's intrinsic instrumental strain noise S_{inst} as well as confusion noise from galactic binaries, S_{gcn} ,

$$S_{\text{noise}}(f) = S_{\text{inst}}(f) + S_{\text{gcn}}(f) \quad (3.2)$$

S_{inst} is in turn given by the detector noise spectrum D_{inst} and signal response function \mathcal{R} ,

$$S_{\text{inst}}(f) = \frac{D_{\text{inst}}(f)}{\mathcal{R}(f)} . \quad (3.3)$$

In the following, we shall now discuss the quantities D_{inst} , \mathcal{R} , and S_{gcn} one after another. The detector noise spectrum can be written as a sum of two stationary contributions [44],²

$$D_{\text{inst}}(f) = \frac{1}{L^2} D_{\text{oms}}(f) + \frac{2}{(2\pi f)^4 L^2} \left[1 + \cos^2\left(\frac{f}{f_*}\right) \right] D_{\text{acc}}(f) . \quad (3.4)$$

Here, $L = 2.5 \times 10^9$ m and $f_* = c/(2\pi L) \simeq 19.09$ mHz denote LISA's arm length and transfer frequency, respectively; D_{oms} and D_{acc} account for the noise in the *optical metrology system* (OMS) (*i.e.*, position noise) and the acceleration noise of a single test mass, respectively,

$$\begin{aligned} D_{\text{oms}}(f) &\simeq (1.5 \times 10^{-11} \text{ m})^2 \left[1 + \left(\frac{2 \text{ mHz}}{f} \right)^4 \right] \text{ Hz}^{-1} , \\ D_{\text{acc}}(f) &\simeq (3 \times 10^{-15} \text{ m s}^{-2})^2 \left[1 + \left(\frac{0.4 \text{ mHz}}{f} \right)^2 \right] \left[1 + \left(\frac{f}{8 \text{ mHz}} \right)^4 \right] \text{ Hz}^{-1} . \end{aligned} \quad (3.5)$$

LISA's signal response function \mathcal{R} describes the response of an equal-arm Michelson interferometer to an incoming GW tensor mode. In the past, one had to rely on semianalytical expressions or numerical techniques to evaluate this function [46–51]; only Ref. [52] recently

²For a recent discussion of nonstationary noise sources for the LISA mission, see Ref. [45].

succeeded in deriving a closed analytical expression for \mathcal{R} . In our analysis, we will use this new analytical result; in particular, we will work with the compact form presented in Ref. [53],

$$\begin{aligned} u^2 \mathcal{R}(u, \gamma) = & s_{2u} \left[s_{\gamma/2}^2 \left(\frac{1}{u} + \frac{2}{u^3} \right) + c_{\gamma/2}^2 \left(2 \text{Si}(2u) - \text{Si}(2u_+) - \text{Si}(2u_-) \right) \right] \\ & + c_{2u} \left[s_{\gamma/2}^2 \left(\frac{1}{6} - \frac{2}{u^2} \right) + c_{\gamma/2}^2 \left(2 \text{Ci}(2u) - \text{Ci}(2u_+) - \text{Ci}(2u_-) + \ln c_{\gamma/2}^2 \right) \right] \\ & - \frac{s_{u_+ - u_-}}{32u s_{\gamma/2}^3} \left(21 - 28 c_\gamma + 7 c_{2\gamma} + \frac{3 - c_\gamma}{u^2} \right) + \frac{c_{u_+ - u_-}}{8u^2 s_{\gamma/2}^2} \left(1 + s_{\gamma/2}^2 \right) \\ & - 2 s_{\gamma/2}^2 \left(\text{Ci}(2u) - \text{Ci}(u_+ - u_-) + \ln s_{\gamma/2} \right) + \frac{3 - c_\gamma}{12} - \frac{1 - c_\gamma}{u^2}, \end{aligned} \quad (3.6)$$

where we introduced the following notation to arrive at an even more compact expression,

$$s_x = \sin(x), \quad c_x = \cos(x), \quad u_\pm = u \pm u \sin\left(\frac{\gamma}{2}\right). \quad (3.7)$$

The independent variables u and γ in Eq. (3.6) represent the GW frequency in units of the transfer frequency, $u = f/f_*$, and the opening angle of the interferometer, respectively. In the case of LISA, which will consist of three spacecraft in an equilateral triangular formation, we have $\gamma = \pi/3$. Finally, Si and Ci in Eq. (3.6) represent sine and cosine integral functions,

$$\text{Si}(x) = \int_0^x dt \frac{\sin(t)}{t}, \quad \text{Ci}(x) = - \int_x^\infty dt \frac{\cos(t)}{t}. \quad (3.8)$$

By making use of Eq. (3.6) instead of, say, an approximate fit function for \mathcal{R} (see, *e.g.*, Ref. [44]), we are able to eliminate all numerical uncertainties in computing S_{inst} . The net effect of this will be small. On the other hand, there is no reason to artificially reduce the precision of our analysis when an exact result for \mathcal{R} is readily available in the literature. For a discussion of the signal response in the case of unequal interferometer arm lengths, which will ultimately correspond to the physical situation during the LISA mission, see also [54, 55].

The last ingredient entering the noise spectrum is the GCN from compact binaries, $S_{\text{gc}}n$. A semianalytical fit function for $S_{\text{gc}}n$ has been worked out in Ref. [37], which estimates the GCN seen by LISA based on the compact-binary population model in Refs. [34, 35],³

$$S_{\text{gc}}n(f) = A \left(\frac{1 \text{ mHz}}{f} \right)^{7/3} \exp \left[- (f/f_{\text{ref}})^\alpha - \beta f \sin(\kappa f) [1 + \tanh(\gamma(f_{\text{knee}} - f))] \right]. \quad (3.9)$$

This fit has been obtained making use of a variant of the BAYESLINE algorithm [56] that applies Markov chain Monte Carlo techniques to sample the entire parameter space of the compact-binary population model. The expression in Eq. (3.9) therefore marginalizes over the parameters of the noise model, which allows us to directly compare and add it to the sky- and polarization-averaged instrumental noise in Eq. (3.3). The overall amplitude A and reference frequency f_{ref} in Eq. (3.9) are fixed at constant values, $A = 9 \times 10^{-38} \text{ Hz}^{-1}$ and $f_{\text{ref}} = 1000 \text{ mHz}$. Meanwhile, the parameters α , β , κ , and γ as well as the frequency f_{knee} , which describes the position of a knee-like feature in the GCN spectrum, depend on LISA's observing

³Here, we correct a typo that appears in Eq. (3) of Ref. [37] as well as in Eq. (14) of Ref. [44]. In both expressions for $S_{\text{gc}}n$, the sign in front of the coefficient β needs to be negative, *i.e.*, $+\beta$ needs to be replaced by $-\beta$. We thank Travis Robson and Neil J. Cornish for a helpful discussion on this point.

Table 1. Parameters appearing in the fit function for the GCN spectrum S_{gcn} in Eq. (3.9) as functions of the collected amount of data t_{data} [37]. Note that Ref. [37] works in units where 1 Hz is set to 1.

t_{data} [yr]	α	β [mHz ⁻¹]	κ [mHz ⁻¹]	γ [mHz ⁻¹]	f_{knee} [mHz]
0.5	0.133	0.243	0.482	0.917	2.58
1.0	0.171	0.292	1.020	1.680	2.15
2.0	0.165	0.299	0.611	1.340	1.73
4.0	0.138	-0.221	0.521	1.680	1.13

time; see Tab. 1. The reason for this is that, as the mission progresses, the increasingly larger amount of data will allow one to successively resolve more and more compact binaries, which can then be individually subtracted from the unresolved GCN background. As a result, the GCN contribution to LISA’s strain noise spectrum, S_{gcn} , decreases as function of t_{data} . In Sec. 4, we will explicitly account for this time dependence of the noise spectrum and consider the four benchmark values that were studied in Ref. [37], $t_{\text{data}} = 0.5, 1.0, 2.0, 4.0$ yr.

4 Sensitivity

The SNR ϱ for given signal and noise spectra Ω_{signal} and Ω_{noise} can be computed as [6, 57, 58],

$$\varrho = \left[t_{\text{data}} \int_{f_{\text{min}}}^{f_{\text{max}}} df \left(\frac{\Omega_{\text{signal}}(f)}{\Omega_{\text{noise}}(f)} \right)^2 \right]^{1/2}. \quad (4.1)$$

This expression is valid for an idealized auto-correlation measurement with perfect noise subtraction, assuming a stochastic, Gaussian, stationary, isotropic, and unpolarized GW background in the weak-signal regime. The SNR in Eq. (4.1) moreover corresponds to the *optimal* SNR that can in principle be achieved when an optimally chosen matched filter is applied to the data. This is reflected in the fact that Eq. (4.1) assumes knowledge of the signal spectrum Ω_{signal} that one actually attempts to measure. The upshot of these caveats is that Eq. (4.1) should be regarded as the theoretical *upper bound* on the expected SNR. If LISA should indeed detect a GW signal from a cosmological phase transition, the actual SNR based on the real data is likely going to be smaller (see, *e.g.*, the χ^2 analysis in Ref. [59]).⁴

The key idea behind the PISC concept is to rewrite the SNR in Eq. (4.1) as follows [1, 2],

$$\varrho = \frac{\Omega_{\text{tot}}(\alpha, \beta/H_*, T_*, v_w)}{\Omega_{\text{pis}}(f_{\text{peak}}, t_{\text{data}}, p, q, n)}, \quad (4.2)$$

where the peak-integrated sensitivity Ω_{pis} follows from integrating over the noise spectrum Ω_{noise} after weighting it with the shape function \mathcal{S} for the acoustic GW signal from a SFOPT,

$$\Omega_{\text{pis}}(f_{\text{peak}}, t_{\text{data}}, p, q, n) = \left[t_{\text{data}} \int_{f_{\text{min}}}^{f_{\text{max}}} df \left(\frac{\mathcal{S}(f/f_{\text{peak}}, p, q, n)}{\Omega_{\text{noise}}(f, t_{\text{data}})} \right)^2 \right]^{-1/2}. \quad (4.3)$$

⁴Another important factor is the efficiency of compact-binary subtraction in the course of the LISA mission. On the one hand, one might not be able to individually resolve and subtract as many compact binaries as initially expected. On the other hand, additional characteristics of the GCN signal, such as its anisotropy and time dependence, might in fact help in its subtraction. We leave a more detailed investigation for future work; in this paper, we are going to follow Refs. [37, 44] and work with the noise model described in Sec. 3.

For a given experiment and fixed shape function, Ω_{pis} can be constructed once and for all. That is, in order to compute the SNR values for a set of benchmark points, it is no longer necessary to carry out the frequency integration in Eq. (4.1) over and over again. Instead, it suffices to construct the experimental PISC in the two-dimensional parameter space spanned by f_{peak} and Ω_{tot} and focus on computing the theoretical predictions for exactly these two observables. Each benchmark scenario can then be represented by its $(f_{\text{peak}}, \Omega_{\text{tot}})$ coordinates in this two-dimensional space, and the corresponding optimal SNR can be identified as the vertical distance Δy between the point $(x, y) = (f_{\text{peak}}, \Omega_{\text{tot}})$ and the PISC of interest. In other words, PISC plots retain the full information on the SNR and encode it on the y axis.

We are now ready to turn to the main part of our analysis and draw our PISC master plot for LISA’s sensitivity to acoustic GWs from a cosmological phase transition; see Fig. 1. In this plot, we show how LISA’s PISC varies for different assumptions regarding the spectral shape of the signal — $p \in \{3, 4, 5\}$, $q \in \{3, 4\}$, $n \in \{1, 2, 3\}$ — and as a function of the observing time t_{data} . In addition, we indicate the $(f_{\text{peak}}, \Omega_{\text{tot}})$ coordinates of all 3720 benchmark points that were studied in Ref. [13]. These benchmark points belong to the following ten models:

1. Dark-sector model featuring a spontaneously broken $U(1)$ gauge symmetry [60]
2. Dark-sector model featuring two gauge-singlet scalars [60]
3. $|H|^6$ and $|H|^8$ operators in the *standard model effective field theory* (SMEFT) [61]
4. Dark-matter model based on gauged and spontaneously broken lepton number [62]
5. Extension of the standard model by a real scalar singlet [1, 63]
6. Extension of the standard model by a \mathbb{Z}_2 -symmetry-protected real scalar singlet [64, 65]
7. Two-Higgs-doublet model with a softly broken \mathbb{Z}_2 symmetry [66–69]
8. Holographic phase transitions in extra-dimensional Randall–Sundrum models [70]
9. Selection of supersymmetric models featuring chiral singlet or triplet fields [71–74]
10. Composite-Higgs models featuring different pseudo-Nambu–Goldstone bosons [75]

More details on these models can be found in Ref. [13] and on the web page of the associated online tool PTPLOT [76], which lists the SFOPT parameters for all 3720 benchmark points.⁵ A characteristic feature of Fig. 1 (see also the enlarged section in Fig. 2) is that it allows us to present the expected SNR values of all benchmark points and models in a single plot. We reiterate that this is infeasible when working instead with model-specific SNR plots on approximate hypersurfaces in the high-dimensional SFOPT parameter space (see Sec. 1).

Figs. 1 and 2 provide a graphical illustration of how varying the observing time t_{data} and spectral shape of the signal affects LISA’s sensitivity reach. For each (p, q, n) tuple, Figs. 1 and 2 show four PISCs that indicate LISA’s sensitivity reach after $t_{\text{data}} = 0.5, 1.0, 2.0, 4.0$ yr (from top to bottom), respectively. The four times six curves for $n = 2$ are drawn explicitly in both figures; the envelopes of all other curves are indicated by gray-shaded bands. We moreover repeat that, for any given benchmark point, the distance between this point and any of the PISCs along the y direction equals the corresponding optimal SNR. This is also illustrated by the ruler in the top-right legend box in Figs. 1, which is true to scale.

⁵We thank the LISA Cosmology Working Group for explicitly giving us permission to use this data.

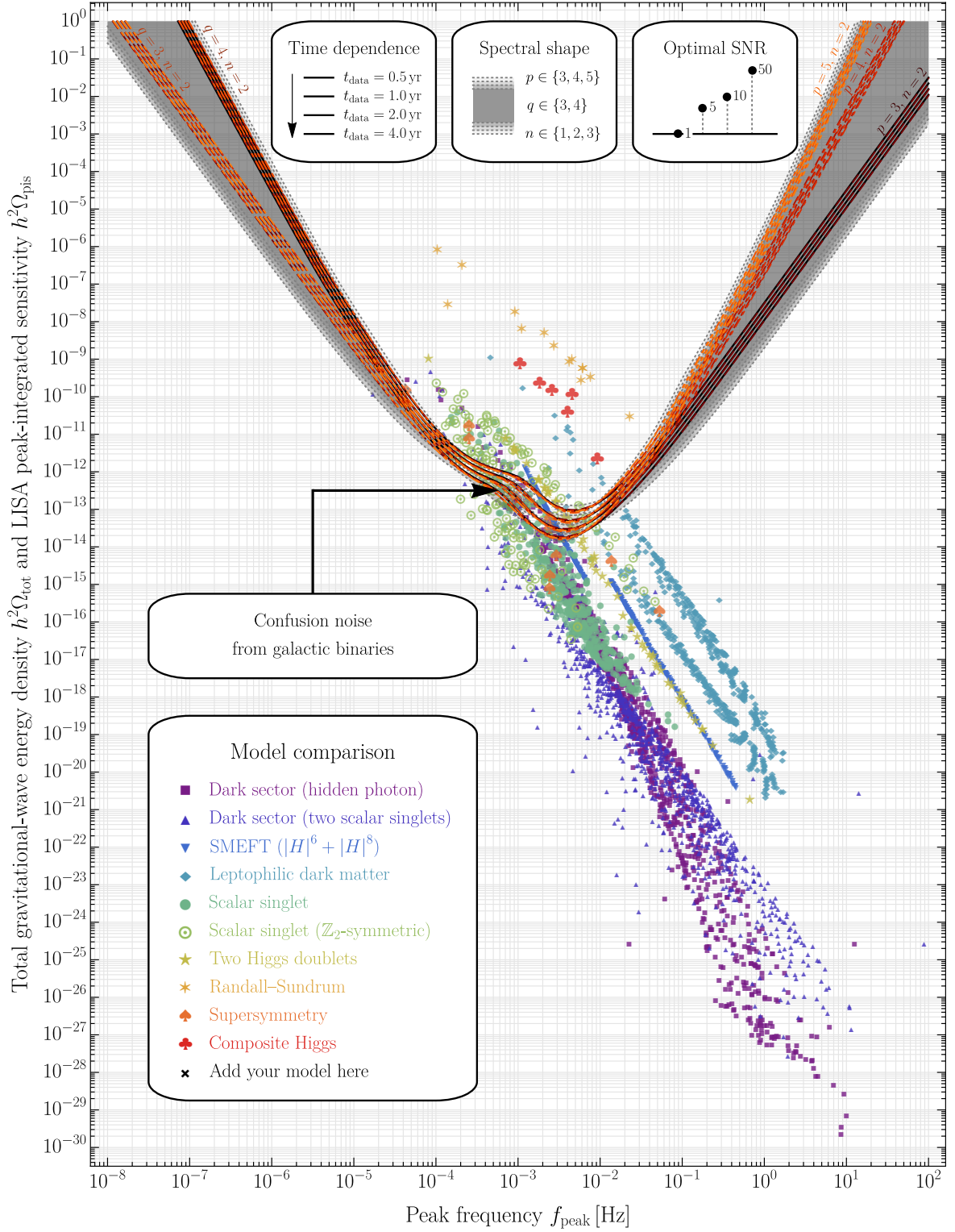


Figure 1. Global picture of LISA’s sensitivity to the acoustic GW signal from a SFOPT. See text.

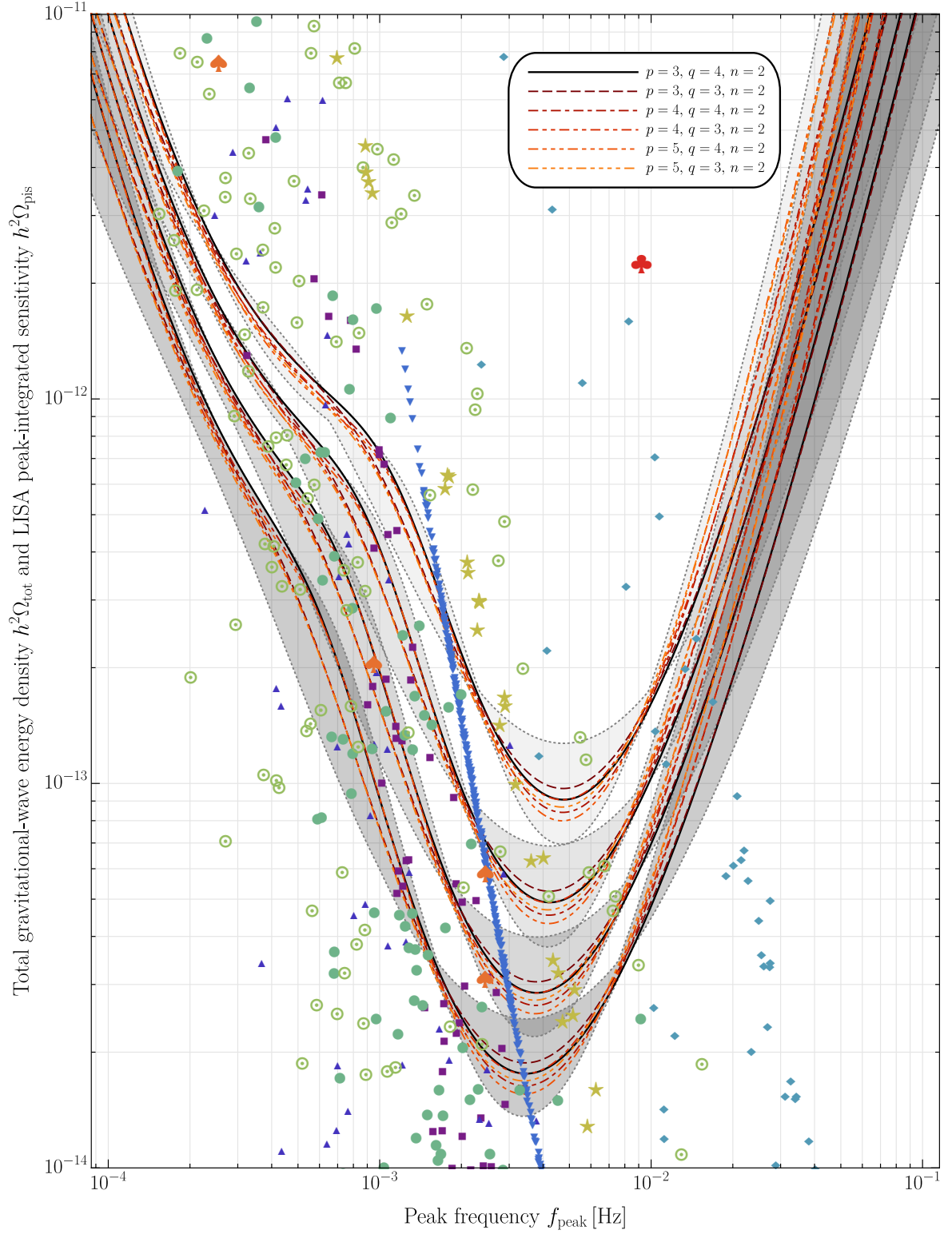


Figure 2. Same as Fig. 1, zoomed into the most relevant region of the $f_{\text{peak}} - \Omega_{\text{tot}}$ parameter space.

In order to quantify the effect of varying the observing time or spectral shape of the signal, we shall now determine the number of benchmark scenarios that surpass an SNR threshold of $\varrho_{\text{thr}} = 10$ in dependence of the parameters p , q , n , and t_{data} . Here, $\varrho_{\text{thr}} = 10$ represents the detection threshold that was identified and used in the analysis of Ref. [12]. Of course, such a counting analysis is not going to replace a proper statistical analysis that would quantify the probability of LISA observing a signal in particular model or class of models. However, given the present state of the art, which amounts to solitary benchmark points and independent collections of model scans, we believe that our simple counting analysis can at least convey a rough impression of the effect of different signal shapes and observing times.

In a first step, we count the total number of above-threshold scenarios without distinguishing between different models; see Fig. 3. The general trend that can be read off from this figure is that, without accounting for GCN, an observing time of $t_{\text{data}} = 0.5$ yr results in roughly 130 observable scenarios, which increases to roughly 250 observable scenarios after an observing time of $t_{\text{data}} = 4.0$ yr. However, accounting for GCN in the analysis, these numbers are reduced by roughly a factor 2.2 and 1.6, respectively, down to roughly 60 observable scenarios for $t_{\text{data}} = 0.5$ yr and roughly 160 observable scenarios for $t_{\text{data}} = 4.0$ yr. The spread in these numbers related to different choices of p , q , and n is generally very small, which is also evident from the sensitivity curves shown in Figs. 1 and 2. In a second step, we repeat our analysis for the standard spectral shape that is described by $(p, q, n) = (3, 4, 2)$; see Fig. 4. Now we count the number of benchmark scenarios above detection threshold for each individual model. Again we find that including GCN has a significant impact on the number of observable benchmark points, although now we see that the effect can be very different from model to model. Extremely strong phase transitions, such as those in Randall–Sundrum and composite-Higgs models, will simply be always observable.⁶ The detectability of other models, on the other hand, significantly improves in the course of the LISA mission. This is, *e.g.*, the case for the \mathbb{Z}_2 -symmetric real-scalar-singlet model, for which many benchmark points lie only slightly above the LISA PISC at the beginning of the mission. These points notably benefit from the improving sensitivity as the collected amount of data increases.

5 Conclusions

In this short note, we presented a global picture of LISA’s sensitivity to acoustic GWs from a SFOPT in the early Universe. Our main results are the PISC plots in Figs. 1 and 2, which retain the complete information on the optimal SNR and visualize LISA’s sensitivity to a broad range of SFOPT scenarios in a compact fashion. We argued that these plots are well suited to collectively study a large number of benchmark points and models at the same time, which we demonstrated by discussing (i) the importance of GCN, (ii) the time dependence of LISA’s PISC, and (iii) the impact of varying the spectral shape of the signal.

To illustrate the characteristic features of our approach, we also reproduced the predictions for all benchmark points and models that were discussed in the second review report by the LISA Cosmology Working Group [13]. Out of the 3720 benchmark points in this dataset, roughly 250 points (*i.e.*, roughly 7%) lead to an optimal SNR above detection threshold after an observing time of $t_{\text{data}} = 4.0$ yr when GCN is neglected. This number is reduced

⁶At present, the description of these scenarios, however, relies on extrapolating the results of numerical simulations that were performed for weak phase transitions, $\alpha \lesssim 1$, across many orders of magnitude in α . The most promising benchmark points in the sample are therefore also the least understood. More work is needed to improve our understanding of the dynamics and GW signature of these extreme phase transitions.

Number of benchmark points with SNR $\varrho > 10$ summed over all models for all (p, q, n) tuples								
(p, q, n)	$t_{\text{data}} = 0.5 \text{ yr}$		$t_{\text{data}} = 1.0 \text{ yr}$		$t_{\text{data}} = 2.0 \text{ yr}$		$t_{\text{data}} = 4.0 \text{ yr}$	
	+ GCN		+ GCN		+ GCN		+ GCN	
(3, 3, 1)	62	132	88	160	116	191	169	235
(3, 3, 2)	58	125	79	156	104	197	159	243
(3, 3, 3)	59	125	77	160	100	199	155	253
(3, 4, 1)	59	127	84	158	108	189	162	235
(3, 4, 2)	57	121	76	153	99	196	150	245
(3, 4, 3)	56	122	73	156	94	199	147	249
(4, 3, 1)	62	132	88	163	113	193	169	240
(4, 3, 2)	61	129	80	159	106	200	162	253
(4, 3, 3)	61	131	80	163	101	208	160	261
(4, 4, 1)	59	130	84	159	108	193	164	236
(4, 4, 2)	59	126	77	159	99	203	156	252
(4, 4, 3)	58	127	76	160	96	209	153	256
(5, 3, 1)	62	134	88	164	112	196	170	242
(5, 3, 2)	62	130	81	165	106	204	167	257
(5, 3, 3)	61	133	80	165	103	213	168	263
(5, 4, 1)	60	130	84	160	106	197	166	240
(5, 4, 2)	61	129	79	162	100	207	161	258
(5, 4, 3)	60	131	78	165	98	213	157	262

Figure 3. Number of benchmark points above detection threshold in dependence of p , q , n , and t_{data} . The color code reflects the spectrum of values in this table, ranging from 56 (red) to 263 (green).

		Number of benchmark points with SNR $\varrho > 10$ per individual model for $(p, q, n) = (3, 4, 2)$							
		$t_{\text{data}} = 0.5 \text{ yr}$		$t_{\text{data}} = 1.0 \text{ yr}$		$t_{\text{data}} = 2.0 \text{ yr}$		$t_{\text{data}} = 4.0 \text{ yr}$	
	Total	+ GCN		+ GCN		+ GCN		+ GCN	
Dark sector (hidden photon)	1000	3	9	5	14	5	16	6	18
Dark sector (two scalar singlets)	1000	4	10	4	11	6	15	10	17
SMEFT ($ H ^6 + H ^8$)	541	0	9	0	23	2	45	28	77
Leptophilic dark matter	540	11	12	12	12	12	13	14	14
Scalar singlet	394	2	11	3	13	5	16	12	20
Scalar singlet (\mathbb{Z}_2 -symmetric)	152	16	39	30	46	38	53	43	59
Two Higgs doublets	62	1	10	2	12	10	16	16	18
Randall–Sundrum	14	14	14	14	14	14	14	14	14
Supersymmetry	11	0	1	0	2	1	2	1	2
Composite Higgs	6	6	6	6	6	6	6	6	6

Figure 4. Number of benchmark points above detection threshold for $(p, q, n) = (3, 4, 2)$. The color code reflects the relative number of observable points, ranging from 0 % (red) to 100 % (green).

by roughly a factor of 2 down to roughly 160 points (*i.e.*, roughly 4 %) when GCN is taken into account following the treatment in Refs. [37, 44] (see Fig. 3). Of course, the situation may vary strongly from model to model (see Fig. 4). In general, we are, however, able to draw two basic conclusions: (i) In most cases, only a small fraction of all benchmark points is above detection threshold; and those benchmark points that manage to surpass the detection threshold often times rely on extrapolating simulation results across many orders of magnitude. (ii) The impact of GCN is nonnegligible and should always be accounted for in phenomenological studies of GWs from a cosmological phase transition. In this work, we did this using the fit function derived in Refs. [37], which marginalizes over the uncertainties of the GCN model. In future work, it would be interesting to refine our analysis based on a more sophisticated treatment of GCN. In summary, we conclude that the GW phenomenology of SFOPTs in the early Universe remains an exciting, but also challenging topic. More work is needed to identify models with good detection prospects, *i.e.*, models where the fraction of accessible benchmark points is above the percent level; and more work is needed to better simulate and understand the phase transitions in these models from a theoretical perspective.

Acknowledgments

I wish to thank Sergei Bobrovskiy, Neil J. Cornish, John Ellis, Felix Giese, Max Hoffmann, Thomas Konstandin, Marek Lewicki, Toby Opferkuch, Travis Robson, Jorinde van de Vis, and David Weir for helpful discussions and comments. I am also grateful to the chairs of the LISA Cosmology Working Group for giving me permission to use the data on ptplot.org. This project has received funding from the European Union’s Horizon 2020 Research and Innovation Programme under grant agreement number 796961, “AxiBAU” (K.S.).

References

- [1] T. Alanne, T. Hugle, M. Platscher, and K. Schmitz, *A fresh look at the gravitational-wave signal from cosmological phase transitions*, *JHEP* **03** (2020) 004, [[arXiv:1909.11356](https://arxiv.org/abs/1909.11356)].
- [2] K. Schmitz, *New Sensitivity Curves for Gravitational-Wave Experiments*, [arXiv:2002.04615](https://arxiv.org/abs/2002.04615).
- [3] K. Schmitz, “*LISA Sensitivity to Gravitational Waves from Sound Waves.*” [http://doi.org/10.5281/zenodo.3837877](https://doi.org/10.5281/zenodo.3837877).
- [4] **LISA**, P. Amaro-Seoane et al., *Laser Interferometer Space Antenna*, [arXiv:1702.00786](https://arxiv.org/abs/1702.00786).
- [5] J. Baker et al., *The Laser Interferometer Space Antenna: Unveiling the Millihertz Gravitational Wave Sky*, [arXiv:1907.06482](https://arxiv.org/abs/1907.06482).
- [6] M. Maggiore, *Gravitational wave experiments and early universe cosmology*, *Phys. Rept.* **331** (2000) 283, [[gr-qc/9909001](https://arxiv.org/abs/gr-qc/9909001)].
- [7] J. D. Romano and N. J. Cornish, *Detection methods for stochastic gravitational-wave backgrounds: a unified treatment*, *Living Rev. Rel.* **20** (2017), no. 1 2, [[arXiv:1608.06889](https://arxiv.org/abs/1608.06889)].
- [8] C. Caprini and D. G. Figueroa, *Cosmological Backgrounds of Gravitational Waves*, *Class. Quant. Grav.* **35** (2018) 163001, [[arXiv:1801.04268](https://arxiv.org/abs/1801.04268)].
- [9] N. Christensen, *Stochastic Gravitational Wave Backgrounds*, *Rept. Prog. Phys.* **82** (2019) 016903, [[arXiv:1811.08797](https://arxiv.org/abs/1811.08797)].
- [10] D. J. Weir, *Gravitational waves from a first order electroweak phase transition: a brief review*, *Phil. Trans. Roy. Soc. Lond. A* **376** (2018), no. 2114 20170126, [[arXiv:1705.01783](https://arxiv.org/abs/1705.01783)].
- [11] A. Mazumdar and G. White, *Review of cosmic phase transitions: their significance and experimental signatures*, *Rept. Prog. Phys.* **82** (2019) 076901, [[arXiv:1811.01948](https://arxiv.org/abs/1811.01948)].
- [12] C. Caprini et al., *Science with the space-based interferometer eLISA. II: Gravitational waves from cosmological phase transitions*, *JCAP* **04** (2016) 001, [[arXiv:1512.06239](https://arxiv.org/abs/1512.06239)].
- [13] C. Caprini et al., *Detecting gravitational waves from cosmological phase transitions with LISA: an update*, *JCAP* **2003** (2020) 024, [[arXiv:1910.13125](https://arxiv.org/abs/1910.13125)].
- [14] M. Hindmarsh, S. J. Huber, K. Rummukainen, and D. J. Weir, *Gravitational waves from the sound of a first order phase transition*, *Phys. Rev. Lett.* **112** (2014) 041301, [[arXiv:1304.2433](https://arxiv.org/abs/1304.2433)].
- [15] J. Giblin, John T. and J. B. Mertens, *Vacuum Bubbles in the Presence of a Relativistic Fluid*, *JHEP* **12** (2013) 042, [[arXiv:1310.2948](https://arxiv.org/abs/1310.2948)].
- [16] J. T. Giblin and J. B. Mertens, *Gravitational radiation from first-order phase transitions in the presence of a fluid*, *Phys. Rev. D* **90** (2014) 023532, [[arXiv:1405.4005](https://arxiv.org/abs/1405.4005)].
- [17] M. Hindmarsh, S. J. Huber, K. Rummukainen, and D. J. Weir, *Numerical simulations of acoustically generated gravitational waves at a first order phase transition*, *Phys. Rev. D* **92** (2015) 123009, [[arXiv:1504.03291](https://arxiv.org/abs/1504.03291)].

- [18] M. Hindmarsh, *Sound shell model for acoustic gravitational wave production at a first-order phase transition in the early Universe*, *Phys. Rev. Lett.* **120** (2018) 071301, [[arXiv:1608.04735](#)].
- [19] M. Hindmarsh, S. J. Huber, K. Rummukainen, and D. J. Weir, *Shape of the acoustic gravitational wave power spectrum from a first order phase transition*, *Phys. Rev.* **D96** (2017) 103520, [[arXiv:1704.05871](#)].
- [20] M. Hindmarsh and M. Hijazi, *Gravitational waves from first order cosmological phase transitions in the Sound Shell Model*, *JCAP* **1912** (2019) 062, [[arXiv:1909.10040](#)].
- [21] A. Kosowsky, M. S. Turner, and R. Watkins, *Gravitational radiation from colliding vacuum bubbles*, *Phys. Rev. D* **45** (1992) 4514.
- [22] A. Kosowsky, M. S. Turner, and R. Watkins, *Gravitational waves from first order cosmological phase transitions*, *Phys. Rev. Lett.* **69** (1992) 2026.
- [23] A. Kosowsky and M. S. Turner, *Gravitational radiation from colliding vacuum bubbles: envelope approximation to many bubble collisions*, *Phys. Rev. D* **47** (1993) 4372, [[astro-ph/9211004](#)].
- [24] M. Kamionkowski, A. Kosowsky, and M. S. Turner, *Gravitational radiation from first order phase transitions*, *Phys. Rev. D* **49** (1994) 2837, [[astro-ph/9310044](#)].
- [25] C. Caprini, R. Durrer, and G. Servant, *Gravitational wave generation from bubble collisions in first-order phase transitions: An analytic approach*, *Phys. Rev. D* **77** (2008) 124015, [[arXiv:0711.2593](#)].
- [26] S. J. Huber and T. Konstandin, *Gravitational Wave Production by Collisions: More Bubbles*, *JCAP* **09** (2008) 022, [[arXiv:0806.1828](#)].
- [27] C. Caprini and R. Durrer, *Gravitational waves from stochastic relativistic sources: Primordial turbulence and magnetic fields*, *Phys. Rev. D* **74** (2006) 063521, [[astro-ph/0603476](#)].
- [28] T. Kahniashvili, A. Kosowsky, G. Gogoberidze, and Y. Maravin, *Detectability of Gravitational Waves from Phase Transitions*, *Phys. Rev. D* **78** (2008) 043003, [[arXiv:0806.0293](#)].
- [29] T. Kahniashvili, L. Campanelli, G. Gogoberidze, Y. Maravin, and B. Ratra, *Gravitational Radiation from Primordial Helical Inverse Cascade MHD Turbulence*, *Phys. Rev. D* **78** (2008) 123006, [[arXiv:0809.1899](#)]. [Erratum: *ibid.* **79** (2009) 109901].
- [30] T. Kahniashvili, L. Kisslinger, and T. Stevens, *Gravitational Radiation Generated by Magnetic Fields in Cosmological Phase Transitions*, *Phys. Rev. D* **81** (2010) 023004, [[arXiv:0905.0643](#)].
- [31] C. Caprini, R. Durrer, and G. Servant, *The stochastic gravitational wave background from turbulence and magnetic fields generated by a first-order phase transition*, *JCAP* **12** (2009) 024, [[arXiv:0909.0622](#)].
- [32] L. Kisslinger and T. Kahniashvili, *Polarized Gravitational Waves from Cosmological Phase Transitions*, *Phys. Rev. D* **92** (2015) 043006, [[arXiv:1505.03680](#)].
- [33] E. Thrane and J. D. Romano, *Sensitivity curves for searches for gravitational-wave backgrounds*, *Phys. Rev.* **D88** (2013) 124032, [[arXiv:1310.5300](#)].
- [34] G. Nelemans and C. Tout, *Reconstructing the evolution of white dwarf binaries: Further evidence for an alternative algorithm for the outcome of the common-envelope phase in close binaries*, *Mon. Not. Roy. Astron. Soc.* **356** (2005) 753, [[astro-ph/0410301](#)].
- [35] S. Toonen, G. Nelemans, and S. Portegies Zwart, *Supernova Type Ia progenitors from merging double white dwarfs: Using a new population synthesis model*, *Astron. Astrophys.* **546** (2012) A70, [[arXiv:1208.6446](#)].
- [36] V. Korol, E. M. Rossi, P. J. Groot, G. Nelemans, S. Toonen, and A. G. Brown, *Prospects for detection of detached double white dwarf binaries with Gaia, LSST and LISA*, *Mon. Not. Roy. Astron. Soc.* **470** (2017), no. 2 1894, [[arXiv:1703.02555](#)].

- [37] N. Cornish and T. Robson, *Galactic binary science with the new LISA design*, *J. Phys. Conf. Ser.* **840** (2017) 012024, [[arXiv:1703.09858](#)].
- [38] T. Littenberg, N. Cornish, K. Lackeos, and T. Robson, *Global Analysis of the Gravitational Wave Signal from Galactic Binaries*, *Phys. Rev. D* **101** (2020) 123021, [[arXiv:2004.08464](#)].
- [39] J. R. Espinosa, T. Konstandin, J. M. No, and G. Servant, *Energy Budget of Cosmological First-order Phase Transitions*, *JCAP* **1006** (2010) 028, [[arXiv:1004.4187](#)].
- [40] F. Giese, T. Konstandin, and J. van de Vis, *Model-independent energy budget of cosmological first-order phase transitions—A sound argument to go beyond the bag model*, *JCAP* **07** (2020) 057, [[arXiv:2004.06995](#)].
- [41] J. Ellis, M. Lewicki, and J. M. No, *On the Maximal Strength of a First-Order Electroweak Phase Transition and its Gravitational Wave Signal*, *JCAP* **1904** (2019) 003, [[arXiv:1809.08242](#)].
- [42] J. Ellis, M. Lewicki, J. M. No, and V. Vaskonen, *Gravitational wave energy budget in strongly supercooled phase transitions*, *JCAP* **1906** (2019) 024, [[arXiv:1903.09642](#)].
- [43] J. Ellis, M. Lewicki, and J. M. No, *Gravitational waves from first-order cosmological phase transitions: lifetime of the sound wave source*, *JCAP* **07** (2020) 050, [[arXiv:2003.07360](#)].
- [44] T. Robson, N. J. Cornish, and C. Liu, *The construction and use of LISA sensitivity curves*, *Class. Quant. Grav.* **36** (2019) 105011, [[arXiv:1803.01944](#)].
- [45] M. C. Edwards, P. Maturana-Russel, R. Meyer, J. Gair, N. Korsakova, and N. Christensen, *Identifying and Addressing Nonstationary LISA Noise*, *Phys. Rev. D* **102** (2020) 084062, [[arXiv:2004.07515](#)].
- [46] S. L. Larson, W. A. Hiscock, and R. W. Hellings, *Sensitivity curves for spaceborne gravitational wave interferometers*, *Phys. Rev.* **D62** (2000) 062001, [[gr-qc/9909080](#)].
- [47] S. L. Larson, R. W. Hellings, and W. A. Hiscock, *Unequal arm space borne gravitational wave detectors*, *Phys. Rev.* **D66** (2002) 062001, [[gr-qc/0206081](#)].
- [48] M. Tinto and M. E. da Silva Alves, *LISA Sensitivities to Gravitational Waves from Relativistic Metric Theories of Gravity*, *Phys. Rev.* **D82** (2010) 122003, [[arXiv:1010.1302](#)].
- [49] A. Blaut, *Angular and frequency response of the gravitational wave interferometers in the metric theories of gravity*, *Phys. Rev.* **D85** (2012) 043005, [[arXiv:1901.11268](#)].
- [50] D. Liang, Y. Gong, A. J. Weinstein, C. Zhang, and C. Zhang, *Frequency response of space-based interferometric gravitational-wave detectors*, *Phys. Rev.* **D99** (2019) 104027, [[arXiv:1901.09624](#)].
- [51] C. Zhang, Q. Gao, Y. Gong, D. Liang, A. J. Weinstein, and C. Zhang, *Frequency response of time-delay interferometry for space-based gravitational wave antenna*, *Phys. Rev.* **D100** (2019) 064033, [[arXiv:1906.10901](#)].
- [52] X.-Y. Lu, Y.-J. Tan, and C.-G. Shao, *Sensitivity functions for space-borne gravitational wave detectors*, *Phys. Rev.* **D100** (2019) 044042.
- [53] C. Zhang, Q. Gao, Y. Gong, B. Wang, A. J. Weinstein, and C. Zhang, *Full analytical formulas for frequency response of space-based gravitational wave detectors*, *Phys. Rev. D* **101** (2020) 124027, [[arXiv:2003.01441](#)].
- [54] G. Wang, W.-T. Ni, and W.-B. Han, *Sensitivity investigation for unequal-arm LISA and TAIJI: the first-generation time-delay interferometry optimal channels*, [arXiv:2008.05812](#).
- [55] M. Vallisneri, J.-B. Bayle, S. Babak, and A. Petiteau, *TDI-infinity: time-delay interferometry without delays*, [arXiv:2008.12343](#).
- [56] T. B. Littenberg and N. J. Cornish, *Bayesian inference for spectral estimation of gravitational wave detector noise*, *Phys. Rev. D* **91** (2015) 084034, [[arXiv:1410.3852](#)].

- [57] B. Allen, *The Stochastic gravity wave background: Sources and detection*, in *Relativistic gravitation and gravitational radiation. Proceedings, School of Physics, Les Houches, France, September 26-October 6, 1995*, pp. 373–417, 1996. [gr-qc/9604033](#).
- [58] B. Allen and J. D. Romano, *Detecting a stochastic background of gravitational radiation: Signal processing strategies and sensitivities*, *Phys. Rev.* **D59** (1999) 102001, [[gr-qc/9710117](#)].
- [59] S. Kuroyanagi, T. Chiba, and T. Takahashi, *Probing the Universe through the Stochastic Gravitational Wave Background*, *JCAP* **1811** (2018) 038, [[arXiv:1807.00786](#)].
- [60] M. Breitbach, J. Kopp, E. Madge, T. Opferkuch, and P. Schwaller, *Dark, Cold, and Noisy: Constraining Secluded Hidden Sectors with Gravitational Waves*, *JCAP* **07** (2019) 007, [[arXiv:1811.11175](#)].
- [61] M. Chala, C. Krause, and G. Nardini, *Signals of the electroweak phase transition at colliders and gravitational wave observatories*, *JHEP* **07** (2018) 062, [[arXiv:1802.02168](#)].
- [62] E. Madge and P. Schwaller, *Leptophilic dark matter from gauged lepton number: Phenomenology and gravitational wave signatures*, *JHEP* **02** (2019) 048, [[arXiv:1809.09110](#)].
- [63] C.-Y. Chen, J. Kozaczuk, and I. M. Lewis, *Non-resonant Collider Signatures of a Singlet-Driven Electroweak Phase Transition*, *JHEP* **08** (2017) 096, [[arXiv:1704.05844](#)].
- [64] P. Huang, A. J. Long, and L.-T. Wang, *Probing the Electroweak Phase Transition with Higgs Factories and Gravitational Waves*, *Phys. Rev. D* **94** (2016) 075008, [[arXiv:1608.06619](#)].
- [65] A. Beniwal, M. Lewicki, J. D. Wells, M. White, and A. G. Williams, *Gravitational wave, collider and dark matter signals from a scalar singlet electroweak baryogenesis*, *JHEP* **08** (2017) 108, [[arXiv:1702.06124](#)].
- [66] G. Dorsch, S. Huber, and J. No, *A strong electroweak phase transition in the 2HDM after LHC8*, *JHEP* **10** (2013) 029, [[arXiv:1305.6610](#)].
- [67] G. Dorsch, S. Huber, K. Mimasu, and J. No, *Echoes of the Electroweak Phase Transition: Discovering a second Higgs doublet through $A_0 \rightarrow ZH_0$* , *Phys. Rev. Lett.* **113** (2014) 211802, [[arXiv:1405.5537](#)].
- [68] G. Dorsch, S. Huber, T. Konstandin, and J. No, *A Second Higgs Doublet in the Early Universe: Baryogenesis and Gravitational Waves*, *JCAP* **05** (2017) 052, [[arXiv:1611.05874](#)].
- [69] G. Dorsch, S. Huber, K. Mimasu, and J. No, *The Higgs Vacuum Uplifted: Revisiting the Electroweak Phase Transition with a Second Higgs Doublet*, *JHEP* **12** (2017) 086, [[arXiv:1705.09186](#)].
- [70] E. Megías, G. Nardini, and M. Quirós, *Cosmological Phase Transitions in Warped Space: Gravitational Waves and Collider Signatures*, *JHEP* **09** (2018) 095, [[arXiv:1806.04877](#)].
- [71] S. J. Huber, T. Konstandin, G. Nardini, and I. Rues, *Detectable Gravitational Waves from Very Strong Phase Transitions in the General NMSSM*, *JCAP* **03** (2016) 036, [[arXiv:1512.06357](#)].
- [72] M. Garcia-Pepin and M. Quiros, *Strong electroweak phase transition from Supersymmetric Custodial Triplets*, *JHEP* **05** (2016) 177, [[arXiv:1602.01351](#)].
- [73] L. Bian, H.-K. Guo, and J. Shu, *Gravitational Waves, baryon asymmetry of the universe and electric dipole moment in the CP-violating NMSSM*, *Chin. Phys. C* **42** (2018) 093106, [[arXiv:1704.02488](#)]. [Erratum: *ibid.* **43** (2019) 129101].
- [74] S. Demidov, D. Gorbunov, and D. Kirpichnikov, *Gravitational waves from phase transition in split NMSSM*, *Phys. Lett. B* **779** (2018) 191, [[arXiv:1712.00087](#)].
- [75] S. Bruggisser, B. Von Harling, O. Matsedonskyi, and G. Servant, *Electroweak Phase Transition and Baryogenesis in Composite Higgs Models*, *JHEP* **12** (2018) 099, [[arXiv:1804.07314](#)].
- [76] **LIGO Cosmology Working Group**, D. Weir. <http://ptplot.org>.